Astronomy & Astrophysics manuscript no. main
October 20, 2025

Simulating the LOcal Web (SLOW) - VI

γ-ray Emission in the Local Universe

Ludwig M. Böss ⋆,[1,2], Ildar Khabibullin[2,3], Daniel Karner[2], Klaus Dolag[2,3], Ulrich P. Steinwandel[3], Elena Hernandez-Martinez[2], and Jenny G. Sorce[4,5]

[1] Department of Astronomy and Astrophysics, The University of Chicago, William Eckhart Research Center, 5640 S. Ellis Ave. Chicago, IL 60637
[2] Universitäts-Sternwarte, Fakultät für Physik, Ludwig-Maximilians-Universität München, Scheinerstr.1, 81679 München, Germany
[3] Max Planck Institute for Astrophysics, Karl-Schwarzschild-Str. 1, D-85741 Garching, Germany
[4] Univ. Lille, CNRS, Centrale Lille, UMR 9189 CRIStAL, F-59000 Lille, France
[5] Université Paris-Saclay, CNRS, Institut d'Astrophysique Spatiale, 91405, Orsay, France

Received XXXX; accepted YYYY

ABSTRACT

Context. Diffuse γ-ray emission from cosmic ray (CR) protons scattering off the gas in the intracluster and intergalactic medium (ICM and IGM) remains out of reach for current observations. Detecting this emission would provide constraints on intergalactic magnetic fields as well as dark matter interaction models.

Aims. We aim to provide estimates for diffuse γ-ray emission in the Fermi-LAT band from galaxy clusters and the cosmic web in the local Universe.

Methods. In this work we show results from the first cosmological MHD simulation with an on-the-fly spectral CR model. We model CR injection at shocks, account for adiabatic energy changes and advection of CR protons, and obtain their γ-ray emissivity directly from the simulated CR energy density and spectra. For this we use constrained initial conditions, which evolve in a field closely resembling that of the local Universe, allowing direct comparison to Fermi-LAT data on massive clusters.

Results. We find CR proton acceleration at all structure formation and accretion shocks in galaxy clusters and cosmic web filaments. These protons provide the basis for diffuse γ-ray emission in these regimes. The absolute value of the diffuse γ-ray emission in our simulation lies a few orders of magnitude below the current upper limits found by Fermi-LAT. Under the assumption of our model, a sensitivity of $F_\gamma < 10^{-11}\ \gamma\ \mathrm{s}^{-1}\ \mathrm{cm}^{-2}$ is required for a detection of diffuse emission in Coma.

Key words. Cosmology: large-scale structure of Universe; Gamma rays: galaxies: clusters

. Introduction

-ray astronomy holds the potential to give insight into a num- er of non-thermal processes in the intra-cluster medium (ICM) nd the intergalactic medium (IGM). On the one hand γ pho- ons emitted by quasars allow obtaining lower limit on the GM magnetic field strength and correlation lengths (e.g. Alves atista & Saveliev 2020; Acciari et al. 2023). These photons old enough energy to produce spontaneous electron-positron airs along their path from a quasar through a cosmic void, to arth. These electron-positron pairs can then couple to the back- round magnetic field and be deflected from their original path. ubsequently, these electrons/positrons can potentially Compton upscatter a CMB photon into the X-ray to γ-ray energy range, and given the right scattering geometry this photon could be observed on Earth with a time-delay relative to the main γ-emission of the source (e.g. Plaga 1995; Neronov & Semikoz 2007, 2009; Chen et al. 2015). Depending on the magnetic field geometry and helicity this could lead to a halo around the point-source of gamma emission, which could be skewed to one side of the source (e.g. Neronov & Semikoz 2009; Alves Batista et al. 2016; Alves Batista & Saveliev 2021). The non-detection of such a signal currently poses a lower limit on magnetic fields in voids of $B_{\mathrm{min}} \approx 10^{-14}$ G (e.g. Acciari et al. 2023).

Direct observation of diffuse γ-ray emission in galaxy clusters on the other hand could provide insight into the relativistic proton component in the ICM (see Bykov et al. 2019, for a recent review). In galaxy clusters, the main mechanism of CR proton production is Diffusive Shock Acceleration (DSA) at shocks driven by mergers during the hierarchical structure formation process (e.g. Brüggen et al. 2012; Brunetti & Jones 2014, for reviews of galaxy cluster shocks). These shocks have been studied in detail in the X-ray band due to the shock-induced density and temperature increase (e.g. Böhringer & Werner 2010, for a review) as well as via the radio emission attributed to efficient CR electron acceleration in the so-called radio relics (see van Weeren et al. 2019, for a review). Due to the inefficient energy-loss mechanisms of relativistic protons (see e.g. Fig. 7 in Brunetti & Lazarian 2007) they should be long-lived and with that be able to be transported across the cluster volume.

These relativistic protons can then interact with the thermal background gas and scatter into $\pi^{0,\pm}$-ons. The neutral π^0 further decays into two γ photons. However, the current lack of a detection of such diffuse emission (see e.g. Ackermann et al. 2014, 2015, 2016) with Fermi-LAT puts a limit of roughly 1% of the thermal energy density on the relativistic proton energy density (however there are indications for diffuse γ-ray emission towards

⋆ e-mail: lboess@uchicago.edu

the Coma cluster by Prokhorov & Churazov 2014; Xi et al. 2018; Adam et al. 2021; Baghmanyan et al. 2022).
This puts strain on most of the theories on the efficiency of proton acceleration at merger shocks in the ICM (see e.g. Kang & Jones 2007; Kang & Ryu 2013) which model CR acceleration efficiencies to match radio observations. Under the assumption that CR proton acceleration is more efficient than CR electron acceleration, this would produce CR proton to thermal pressure ratios of up to 20% (see Wittor 2021, for a recent review).
More recent models include the shock obliquity, the angle between shock propagation and background magnetic field, as it has been shown that different obliquities drive different kinds of plasma instabilities which favor either proton or electron acceleration (e.g. Caprioli & Spitkovsky 2014; Ha et al. 2018; Ryu et al. 2019). Given that protons are found to be most efficiently accelerated at quasi-parallel shocks, and observations of radio relic polarisation (e.g. Stroe et al. 2013, 2016; Di Gennaro et al. 2018) as well as simulations (e.g. Wittor et al. 2017; Banfi et al. 2020; Böss et al. 2024) indicate that a large fraction of merger shocks are quasi-perpendicular, this would make merger shocks inefficient at accelerating CR protons, helping to alleviate this problem.
Previous studies have found that with an acceleration efficiency η of up to 50%, significantly above the currently favored efficiencies, detection of diffuse γ-ray emission is just out of reach of Fermi-LAT (Pinzke & Pfrommer 2010; Pinzke et al. 2011). More recent simulations by Vazza et al. (2016) showed that the acceleration efficiency should be of the order $\eta \sim 10^{-3}$ to avoid disagreement with the non-detection by Fermi-LAT. This was followed up by Ha et al. (2020) with the most recent Mach number dependent DSA parametrization of Ryu et al. (2019) which gives a range of $\eta \approx 10^{-3} - 10^{-2}$ for weak intra-cluster shocks with sonic Mach number $\mathcal{M}_s \sim 2.25 - 5$. They equally find that this level of efficiency is in agreement with the current upper limits by Fermi-LAT.
However, none of these simulations explicitly follow the CR proton distribution functions within the simulation but follow either a total energy budget of CRs without explicit information on the spectral slope, or model a CR spectrum in post-processing (but see e.g. Girichidis et al. 2020; Hopkins et al. 2022; Werhahn et al. 2023, for spectral approaches in galaxies). It is therefore worth revisiting this problem in current state-of-the-art simulations.
For this work, we employ the first simulation of a CR-MHD simulation of a 500 h^{-1} cMpc constrained cosmological volume with an on-the-fly Fokker-Planck solver to model CR proton and electron acceleration (and re-acceleration) at shocks, adiabatic changes, and energy losses due to synchrotron emission and inverse Compton scattering off CMB photons.
We presented the results of this simulation related to synchrotron emission from the Cosmic Web in Böss et al. (2024), henceforth Paper I. In this work, we will focus on the CR proton component of the same simulation to study the expected γ-ray emission from galaxy clusters while accounting for the interplay of CR proton acceleration at accretion shocks, their advection within the ICM, and re-acceleration by merger shocks. This is a pathfinder simulation in the adiabatic limit of structure formation (3072^3 particles, 30 million CPUh).
The paper is structured as follows: In Section 2 we will describe the simulation and the code modules employed for this work, as well as our modeling of γ-ray emission by π-on decay from CR proton scattering. Section 3 contains our predictions of γ-ray emission for the full sky via this process. In Section 4, we show the γ luminosity in comparison to the Fermi-LAT limits and compare the spectra of some prominent clusters to observations in Section 5.2. Section 6 contains a discussion of numerical constraints and choice of CR injection parameters. Finally, Section 7 contains our conclusions and a summary of our work.

2. Methods

2.1. Initial Conditions

We use the same simulations as in Paper I, hence we will only present a brief summary of the initial conditions and refer the interested reader again to Sorce (2018); Dolag et al. (2023). These initial conditions are constrained based on galaxy distance modulus and observational redshift, thus peculiar velocity from the CosmicFlows-2 distance modulus survey (Tully et al. 2013). By using a Wiener Filter algorithm (Zaroubi et al. 1995, 1998) and applying several reconstruction steps (Doumler et al. 2013a,b,c; Sorce et al. 2014; Sorce 2015; Sorce et al. 2017; Sorce & Tempel 2017, 2018) a density field of the local Universe is constructed at the initial redshift, using the constrained realization algorithm by Hoffman & Ribak (1991). Usable initial conditions at the desired resolution are then constructed, using the Ginnungagap software[1]. The simulation used in this work is a cosmological box with a side length of $L = 500h^{-1}$ cMpc, centered on the Milky Way. Throughout this work we use a *Planck* cosmology (Planck Collaboration et al. 2014) with matter densities $\Omega_m = 0.307$ and $\Omega_{baryon} = 0.048$, a cosmological constant of $\Omega_\Lambda = 0.692$ and the Hubble parameter $H_0 = 67.77$ km s^{-1} Mpc^{-1}.

2.2. Simulation Code

The simulation was run using OpenGadget3 (Groth et al. 2023), a cosmological Tree-SPH code based on Gadget2 (Springel 2005).
Gravity in OpenGadget3 is solved using a Barnes-Hut tree at short range and a particle-mesh (PM) grid for long-range forces. We employ an updated smoothed particle hydrodynamics (SPH) implementation (Beck et al. 2016) with a spatially and time-dependent high-resolution shock-capturing scheme (Dolag et al. 2005b; Cullen & Dehnen 2010), a Wendland C_4 kernel with 200 neighbors and bias correction (as introduced in Dehnen & Aly 2012), and a high-resolution maximum entropy scheme in the form of thermal conduction (Jubelgas et al. 2004; Arth et al. 2014).
The magneto-hydrodynamics (MHD) solver was presented in Dolag et al. (2009). We also include non-ideal MHD in the form of magnetic diffusion and dissipation as introduced in Bonafede et al. (2011). Divergence of the magnetic field arising from numerical truncation errors is cleaned via the hyperbolic cleaning scheme introduced by Tricco et al. (2016).
Shock properties needed for CR acceleration are captured on the fly with the algorithm described in Beck et al. (2016).

2.3. Cosmic Ray Model

As in Paper I, we use the on-the-fly Fokker-Planck solver Crescendo introduced in Böss et al. (2023b) to include Cosmic Rays in our simulation. Crescendo models the population of CR protons and electrons as piecewise power laws in momentum space and evolves their distribution function in time by

[1] https://code.google.com/p/ginnungagap/

solving the diffusion-advection equation in the two-moment approach, following Miniati (2001). We account for injection at shocks following diffusive shock acceleration (DSA), adiabatic changes due to expansion/contraction of the surrounding thermal gas, and energy losses of electrons due to synchrotron emission and inverse Compton (IC) scattering off CMB photons. This reduces the CR transport equation to

$$\frac{Df(p,\mathbf{x},t)}{Dt} = \left(\frac{1}{3}\nabla\cdot\mathbf{u}\right)p\frac{\partial f(p,\mathbf{x},t)}{\partial p} \tag{1}$$

$$+\frac{1}{p^2}\frac{\partial}{\partial p}\left(p^2\sum_l b_l f(p,\mathbf{x},t)\right) \tag{2}$$

$$+ j(\mathbf{x},p,t). \tag{3}$$

where $\sum_l b_l$ is the sum of all radiative loss mechanisms and $j(\mathbf{x}, p, t)$ is the source term. Protons are considered in the dimensionless momentum range $\hat{p} \equiv \frac{p}{m_p c} \in [0.1, 10^5]$. We discretized the populations with 6 bins (1/dex). CR acceleration is modeled following the DSA model by Ryu et al. (2019) and the shock obliquity-dependent efficiency model by Pais et al. (2018). We inject the fraction of shock energy which is available for CR acceleration into the full momentum range of the CR population as a single power law following a linear DSA slope at a fixed electron to proton energy ratio of $K_{\rm ep} = 0.01$. The fixed injection momentum of $\hat{p}_{\rm inj} = 0.1$ is a compromise between typical injection momenta of $\hat{p}_{\rm inj} \sim 0.01$ for accretion shocks and $\hat{p}_{\rm inj} \sim 1$ for merger shocks in the ICM (see bottom panel of Fig. 8 in Ha et al. 2023). For this run, we use closed boundary conditions at the lower end of the distribution function, as it provides more numerical stability and mimics low-momentum cooling on adiabatic compression, which is not explicitly included in this simulation. CR diffusion is not included as its cost is computationally prohibitive at the scale of this simulation. Further, recent work by Reichherzer et al. (2025) indicates that CRs can be efficiently confined in the ICM, which reduces their effective diffusion coefficient by four orders of magnitude. Under these assumptions, advection is the dominant transport process of CRs, which is implicitly included due to the Lagrangian nature of our code.

2.4. Gamma-Ray Emission

2.4.1. Gamma-Ray Emission from a Proton Spectrum

We compute the γ-ray emission directly from the distribution functions of CR protons obtained from the on-the-fly Fokker-Planck solver, without any further assumptions for gas particles that do not contain a CR population.
For γ-ray emission in the range of 100 MeV to 100 GeV, the decay of π^0 mesons is the dominating channel, with Bremsstrahlung and inverse Compton up-scattering of background photons being sub-dominant by roughly an order of magnitude (see Fig. 13 in Yang et al. 2018). To model the γ-ray emission by π^0-decay we closely follow the approach by Werhahn et al. (2021) and compute the source function for a given γ-photon energy E_γ in units of photons GeV^{-1} s^{-1} cm^{-3} as

$$q_\gamma(E_\gamma) = 4\pi c\, n_H \int_{\hat{p}_{\rm thr}}^{\hat{p}_{\rm max}} {\rm d}\hat{p}\;\; \hat{p}^2\; f(\hat{p})\; \frac{{\rm d}\sigma_\gamma(E_\gamma,\hat{p})}{{\rm d}E_\gamma} \tag{4}$$

where n_H is the number density of hydrogen of the gas particle, $\hat{p}_{\rm thr}$ is the threshold momentum for π^0 production, $\hat{p}_{\rm max}$ is the maximum momentum of the distribution function $f(\hat{p})$ in dimensionless momentum space and

$$\frac{{\rm d}\sigma_\gamma(E_\gamma,\hat{p})}{{\rm d}E} = A_{\rm max}(T_p(\hat{p}))\; F(T_p(\hat{p}), E_\gamma) \tag{5}$$

is the differential γ-ray cross-section as parametrized in Kafexhiu et al. (2014). Here E_γ is the photon energy and $T_p(\hat{p})$ is the kinetic energy of the protons. $A_{\rm max}(T_p(\hat{p}))$ describes the peak of the differential cross section and $F(T_p(\hat{p}), E_\gamma)$ parameterizes the fit to the simulated γ-ray spectrum.
We use their fit to the Geant4 data and integrate Eq. 4 by solving the contribution of each momentum bin individually, accounting for partially filled bins between $\hat{p}_{\rm thr}$ and $\hat{p}_i$.
From Eq. 4 we can obtain an emissivity per photon energy E_γ in units [γ s^{-1} cm^{-3}] from

$$j_\gamma(E_\gamma) = E_\gamma\, q_\gamma \quad . \tag{6}$$

Eq. 4 relates to the total photon flux in units [γ s^{-1} cm^{-2}] for a given energy band $E \in [E_1, E_2]$ via

$$F_\gamma = \frac{1}{4\pi d^2}\int_\Omega {\rm d}V \int_{E_1}^{E_2} {\rm d}E\; q_\gamma \tag{7}$$

with d being the distance from the emitting region to the observer, and its luminosity in units [erg s^{-1}] via

$$L_\gamma = \int_V {\rm d}V \int_{E_1}^{E_2} {\rm d}E\; E\; j_\gamma \tag{8}$$

where V is the volume of the emitting region, in our case the volume of an SPH gas particle with a CR proton population. The emissivity per particle across the whole observational band is found by omitting the volume integral in Eq. 8. For details on the calculation of q_γ within our model and tests, see App. A and App. B, respectively.

2.4.2. Analytic Model for Gamma-Ray Emission

To compare to previous work in the literature, we compute the γ-ray emission following the analytic model by Pfrommer & Enßlin (2004). They derive the source function of γ-rays from a power-law energy spectrum of protons with slope α_p as

$$q_\gamma(E_\gamma)\,{\rm d}E_\gamma\,{\rm d}V \approx c\sigma_{\rm pp} n_H \tilde{n}_{\rm CR}\frac{2^{4-\alpha_\gamma}}{3\alpha_\gamma} \tag{9}$$

$$\times\left(\frac{m_{\pi^0}c^2}{\rm GeV}\right)^{-\alpha_\gamma}\left[\left(\frac{2E_\gamma}{m_{\pi^0}c^2}\right)^{\delta_\gamma}+\left(\frac{2E_\gamma}{m_{\pi^0}c^2}\right)^{-\delta_\gamma}\right]^{\frac{-\alpha_\gamma}{\delta_\gamma}} \tag{10}$$

$$\times\frac{{\rm d}E_\gamma}{\rm GeV}{\rm d}V \tag{11}$$

where $\sigma_{\rm pp} = 32\times(0.96+e^{4.4-2.4\alpha_\gamma})$ mbarn is the effective cross section for the pp-process, $\alpha_\gamma = 4.3(\alpha_p - 1/2)$ is the slope of the γ-ray spectrum and $\delta_\gamma = 0.14\alpha_\gamma^{-1.6} + 0.44$ is the shape parameter. The CR proton number density $\tilde{n}_{\rm CR}$ relates to the thermal energy density $\epsilon_{\rm th}$ via Eq. 8 in Pfrommer & Enßlin (2004) as

$$\tilde{n}_{\rm CR} = X_{\rm cr}\epsilon_{\rm th}\frac{2(\alpha_p-1)}{m_p c^2}\left(\frac{m_p c^2}{\rm GeV}\right)^{\alpha_p-1}\left[\mathcal{B}\left(\frac{\alpha_p-2}{2},\frac{3-\alpha_p}{2}\right)\right]^{-1} \tag{12}$$

where $\mathcal{B}(x,y)$ is the beta-function and $X_{\rm cr} = \frac{P_{\rm cr}}{P_{\rm th}}$ is the CR proton to thermal pressure ratio.

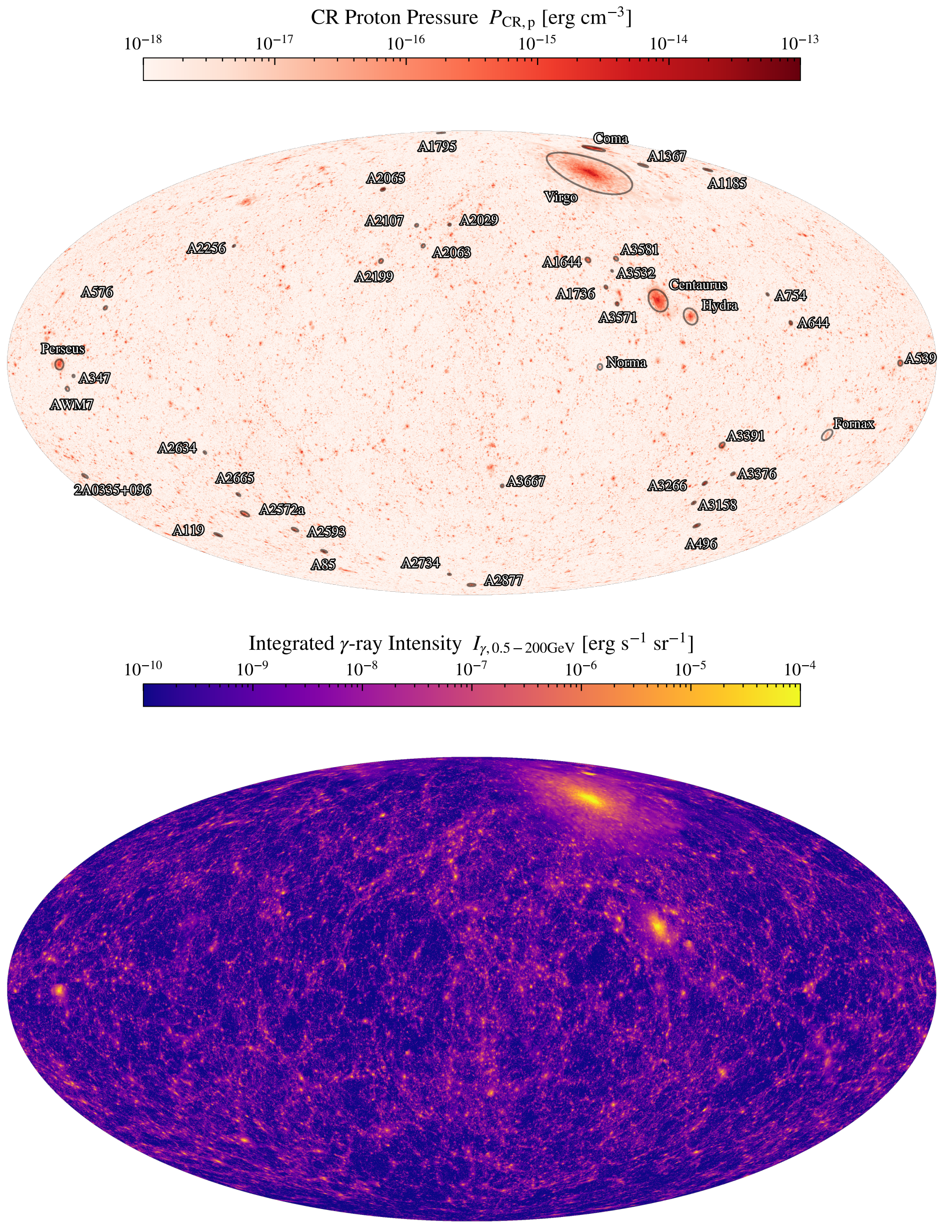

Fig. 1. Full-sky projection in galactic coordinates of simulation box.
Top: CR proton pressure component as the mean value along the line of sight between $r = 10 - 300$ Mpc. This shows predominantly the total injected proton component with adiabatic compression as it settles into the higher-density regions of clusters and filaments. Circles indicate the projected r_{vir} of each of the labeled cluster matches.
Bottom: Integrated γ-ray intensity obtained by integrating over the CR proton spectra according to Eq. 8 in the Fermi-LAT band $E_\gamma \in [0.5 - 200]$ GeV.

3. Full-Sky Projections

As in Paper I, we will first focus on the morphological analysis of the results. For this, we again mapped the simulated SPH quantities on a HealPix sphere (Górski et al. 2005; Dolag et al. 2005a). We chose the same observer view as in Dolag et al. (2023) to match the position of the simulated and observed clusters in our full-sky projection as closely as possible. Full-sky projections are performed for the output at $z = 0$.

3.1. Cosmic Ray Protons

CR protons (CRps) experience hardly any energy losses in the environments of galaxy clusters and cosmic web filaments. The main energy loss mechanism for the overall energy density of CR protons are Coulomb losses due to interaction with the background thermal gas. In galaxy clusters, the cooling time of low-momentum protons is of the order of the Hubble time (e.g. Blasi et al. 2007) and therefore of little importance to the overall evolution of the proton spectra. This holds even more so in the extremely low-density environment of cosmic web filaments.
In Fig. 1 we show the mean CR proton pressure along the line-of-sight from the center up to a radial distance of 300 Mpc within the simulation. We cut at this radius to avoid projection effects by the box corners. Labels indicate the cross-identified clusters from Hernández-Martínez et al. (2024), and the circles indicate the projected virial radius of each cluster.
We find a population of CR protons injected by merger and accretion shocks in all cosmic structures. These protons are advected through the cluster and filament volume, setting into large halos and tracing the cosmic web filaments. In galaxy cluster, we find populations of CR protons that extend up to the virial radius. Beyond that most, if not all, clusters show a faint halo of CR protons even far beyond the virial radius, filling the volume between the virial radius and the virial shock, which has been pushed further from the virial radius by internal merger shocks (see Zhang et al. 2020a,b). The same holds for cosmic web filaments, where we find CR proton populations closely following the cosmological structure. As in the case of clusters, we find extended regions of CR protons around cosmic web filaments.

3.2. Gamma-Ray Emission

As CR protons settle into high-density regions in the cluster center and filaments, they can collide inelastically with the thermal background protons and produce π^0-ons. We model their surface brightness in the energy band observable by Fermi-LAT $E_\gamma \in [0.5 - 200]$ GeV in the lower panel of Fig. 1. Note that this is the integrated intensity, not flux, and not corrected for cosmological distance. This allows us to make estimates of relative brightness between peak emission in clusters and filaments in general and disregard the actual distance to the individual clusters.

In general, we find similar central surface brightness for most of the visible galaxy clusters. They reach central values of $S_\gamma = 10^{-9} - 10^{-8}$ erg s^{-1} cm^{-2}, and decrease by 2-3 orders of magnitude towards $r_{\rm vir}$. Diffuse emission in filaments and around galaxy clusters lies 4-5 orders of magnitude below the central peak, making detection in this regime highly unlikely in the near future.

Similarly to the synchrotron radio emission of CR electrons, we can see the effects of shock acceleration. This is especially evident in the shock in the Perseus cluster, to the left of the map. We will study the γ-ray emission from merger shocks in upcoming work, using higher resolution zoom-in initial conditions.

4. Fermi-LAT Limits

In Fig. 2 we show the comparison of our simulation to the upper limits by Ackermann et al. (2014). The top panel shows the ratio between thermal pressure and CR proton pressure $X_{\rm cr} = \frac{P_{\rm CR,p}}{P_{\rm th}}$. Dots indicate the pressure ratio averaged over the whole cluster volume within r_{200}, while crosses indicate the ratio when only accounting for gas particles that also contain a CR proton population. We further define a rescaling factor χ as the ratio between these two pressure ratios

$$\chi = \frac{X_{\rm CR}(P_{\rm CR} > 0)}{X_{\rm CR}} \tag{13}$$

This can be understood as an upper limit within our pure shock acceleration framework for CR protons. Lines indicate the logarithmic average of the respective values. Please note that $P_{\rm CR,p}$ can only be considered as a lower limit, due to our approach of solving the distribution function in the ultra-relativistic limit. In the range of $\hat{p} \in [0.1, 1.0)$, this is not an exact approximation, leading to an underestimation of the pressure (see discussion in Girichidis et al. 2020).

We find that for the most massive clusters, the volume-averaged ratio between CR and thermal pressure lies 2-3 orders of magnitude below the currently observed limits. This is driven by only a fraction of the gas in the simulation carrying a CR population, which is a direct result of our model for CR acceleration (we will discuss this in more detail in Sec. 6.1). Considering only the average within gas particles that do carry a CR population (crosses in Fig. 2) pushes the average pressure ratio to within 1-2 orders of magnitude of current limits. This is in line with analytic solutions of our employed CR acceleration model (see Fig. 5 in Böss et al. 2023b) when taking into account that most shocks show a shock oliquity $\theta_B \gg 0°$ (see Fig. 13 in Paper I).

The middle panel shows the γ-ray flux within r_{200} as calculated at the same viewpoint used for the full-sky projections in Dolag et al. (2023). We find that the flux in the most massive clusters is 3-4 orders of magnitude below the upper limits found in Pinzke et al. (2011); Ackermann et al. (2014).

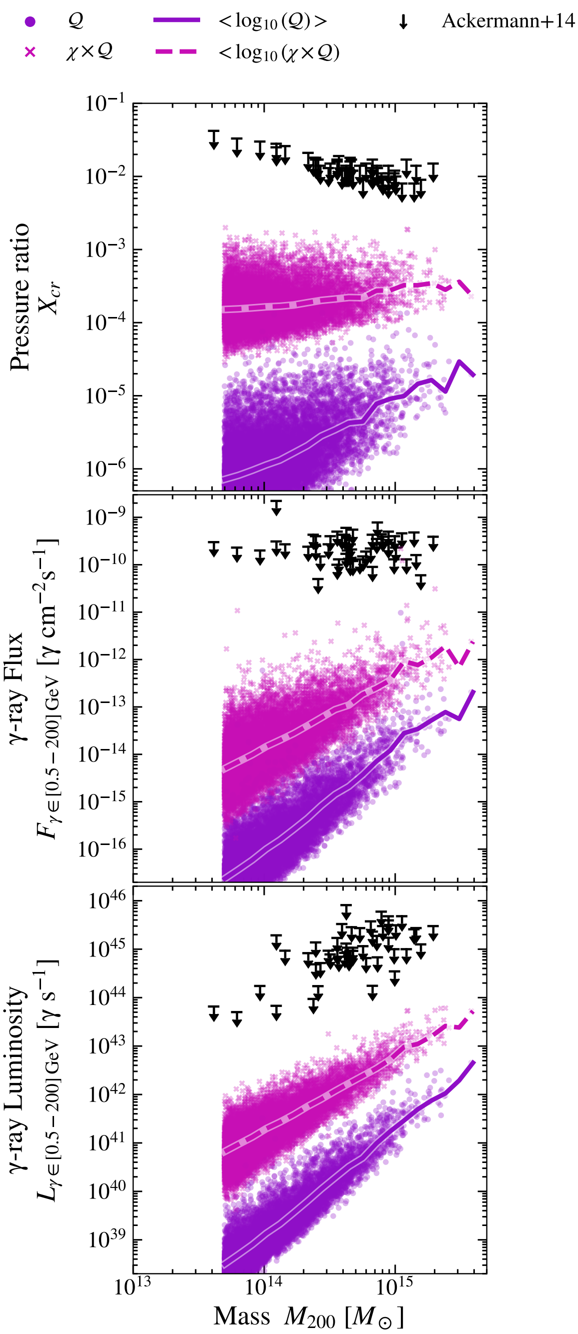

Fig. 2. Results for clusters and groups in the simulation box with a virial mass $M_{\rm vir} > 5 \times 10^{13} M_\odot$. Top panel: CR proton to thermal pressure ratio obtained in the momentum range $\hat{p} \in [0.1, 10^5]$. Middle panel: γ-ray flux obtained at the position of our point of view in Fig. 1 in the energy band $\gamma \in [0.5 - 200]$ GeV. Bottom panel: γ-ray luminosity in the same energy band. In all panels, dots represent the respective quantity Q as obtained from the simulation. Crosses indicate the same quantity upscaled by the ratio between $X_{\rm CR}$ in the whole cluster volume and $X_{\rm CR}$ only in particles that contain a CR population.

To exclude the impact of differences between simulated and observed distances to clusters, we convert the observed γ-ray flux to an intrinsic luminosity by using the reported redshifts in Ackermann et al. (2014) (similar to Ha et al. 2020). Similar to the pressure ratio we find a total luminosity 2-3 orders of magnitude below the observational limit.

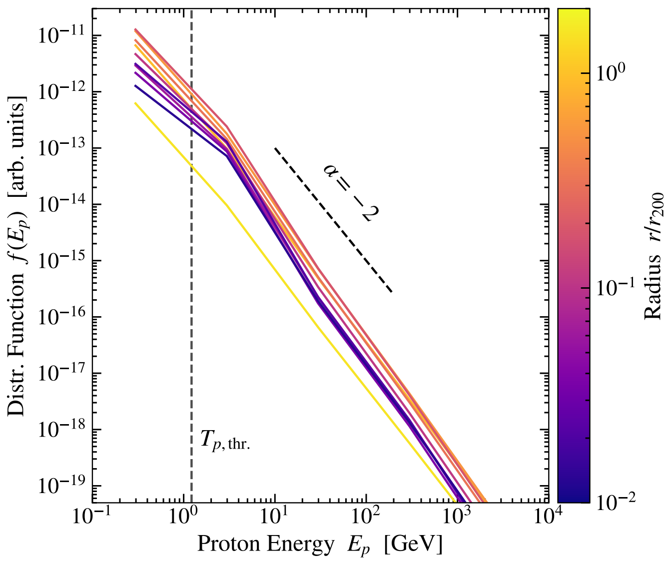

Fig. 3. Mean distribution function in energy space, within our Coma cluster replica. We bin the spectra in 20 radial bins indicated by the different colors. The vertical dashed line indicates the threshold energy beyond which protons can be scattered into π^0-ons.

We find that the reason for this discrepancy is two-fold:
One reason is the numerical behavior of our shock finder. As discussed in Paper I, our shock finder is resolution-limited at this resolution level. This means that we do not capture all shocks, especially in the low Mach number regime inside galaxy clusters. These shocks should contribute significantly to the γ-ray emission in galaxy clusters, as the protons accelerated at these shocks can be advected through the cluster volume. Since γ-ray emission scales linearly with thermal gas density, observability is biased towards the denser ICM, rather than the diffuse ICM, where our shock finder performs better. In addition, due to our shock obliquity-dependent acceleration model and the bias towards high obliquity shocks due to the alignment of the magnetic field with the shock surface over the shock passage, we artificially suppress proton acceleration (see Fig. 9 in Paper I). We will discuss the impact of the shock finder performance on our findings in more detail in Sec. 6.1.
The second reason can be seen in Fig. 3. Here, we show the distribution function of the protons in energy space, color-coded by their distance from the center in our simulated Coma cluster replica.
We find flat spectra in the outskirts of the cluster seen in the bright yellow line, approaching a power law with index $\alpha = -2$. This stems from strong shocks in the cluster periphery, caused by accretion and outward-moving merger shocks. As we move further inside the cluster, shown with increasingly darker lines, we observe two behaviors.
One, the spectra get steeper, since these protons have been accelerated by weaker shocks, typically $\mathcal{M}_s \sim 2-4$ in cluster centers (e.g. Ryu et al. 2003; Vazza et al. 2011; Kang & Ryu 2013; Skillman et al. 2013; Schaal & Springel 2015; Banfi et al. 2020).
Second, the lowest energy bin flattens due to adiabatic compression and our closed lower boundary of the spectrum. This shifts protons to higher momentum bins, without allowing for an influx of protons from the supra-thermal pool. With these steeper spectra, a larger fraction of the total energy density resides in the lower momentum bins. So less energy in these bins leads to significantly less total pressure. This is, however, independent of the γ-ray emission since the threshold energy for π^0-on production, as indicated by the horizontal dashed line, lies at 1.22 GeV and with that beyond the flattened bin.

5. Coma, Virgo and Perseus Clusters

Next, we want to focus on the γ-ray emission from the reproductions of Coma, Virgo, and Perseus clusters in our simulation. For a discussion of the match between simulated and observed clusters, see Hernández-Martínez et al. (2024).

5.1. Surface Brightness

In Fig. 4 we show the γ-ray surface brightness of our cluster replicas. We compute the surface brightness by integrating over Eq. 4 in the energy range $E_\gamma \in [0.2 - 300]$ GeV. Each panel has a width equivalent to $3r_{\mathrm{vir}}$ of the respective cluster. The top panels show the clusters at the resolution of the simulation. Bottom panels are smoothed with a Gaussian beam corresponding to the single photon angular resolution at 1 GeV of $\theta = 0.6°$ of the Fermi-LAT instrument (Atwood et al. 2009). We show the size of this angle in the lower left corner of the images for the redshifts of the observed cluster counterparts.
Our Coma cluster is the dynamically most active of the four clusters shown. It is in the process of undergoing a merger, driving two shocks in the horizontal direction. These shocks accelerate CR protons and exhibit γ-ray surface brightness roughly 1.5 orders of magnitude below the central peak. We also find evidence for CR acceleration at the center, due to small internal shocks, which show the highest surface brightness in Coma. Due to the angular resolution of Fermi-LAT, these structures would not be distinguishable; however, as can be seen in the bottom panel.
Virgo, on the other hand, is a relatively relaxed cluster in our simulation, with no strong ongoing merger activity (see Lebeau et al. 2024, for a detailed study of our Virgo replica). This leads to a more peaked central emission, with a steeper decline in surface brightness towards the outskirts of the cluster.
Our Perseus replica is in the process of a minor merger with a large impact parameter, where a small sub-halo on a highly eccentric orbit drives a shock wave in Perseus' periphery (akin to the main merger geometry in Böss et al. 2023a). The shock can be seen to the top-right of the image, with the substructure driving the shock not visible in the γ-ray image. This ongoing merger activity leads to an overall more perturbed cluster and more extended γ-ray emission than in Virgo.
Nonetheless, we find that all clusters in our set exhibit at least some diffuse γ-ray emission in their ICM, which is tightly linked with their mass and dynamical state.

5.2. Spectra

In Fig. 5 we show the integrated flux spectra of our Coma, Virgo, and Perseus cluster replicas. The top panels show the flux spectrum, obtained by the particles and using the distance between cluster and viewpoint for the full-sky images, while the lower panels show the spectral slope of the γ-ray spectrum obtained between neighboring photon energy bins. Solid lines show our results, and error bars show observational upper limits, where available. For Coma, we compare to the results by Xi et al. (2018); Adam et al. (2021); Baghmanyan et al. (2022). Upper limits for Virgo are provided by Ackermann et al. (2015); H. E. S. S. Collaboration et al. (2023) and for Perseus by Aleksić et al. (2010, 2012); Abe et al. (2024). Dashed and dotted

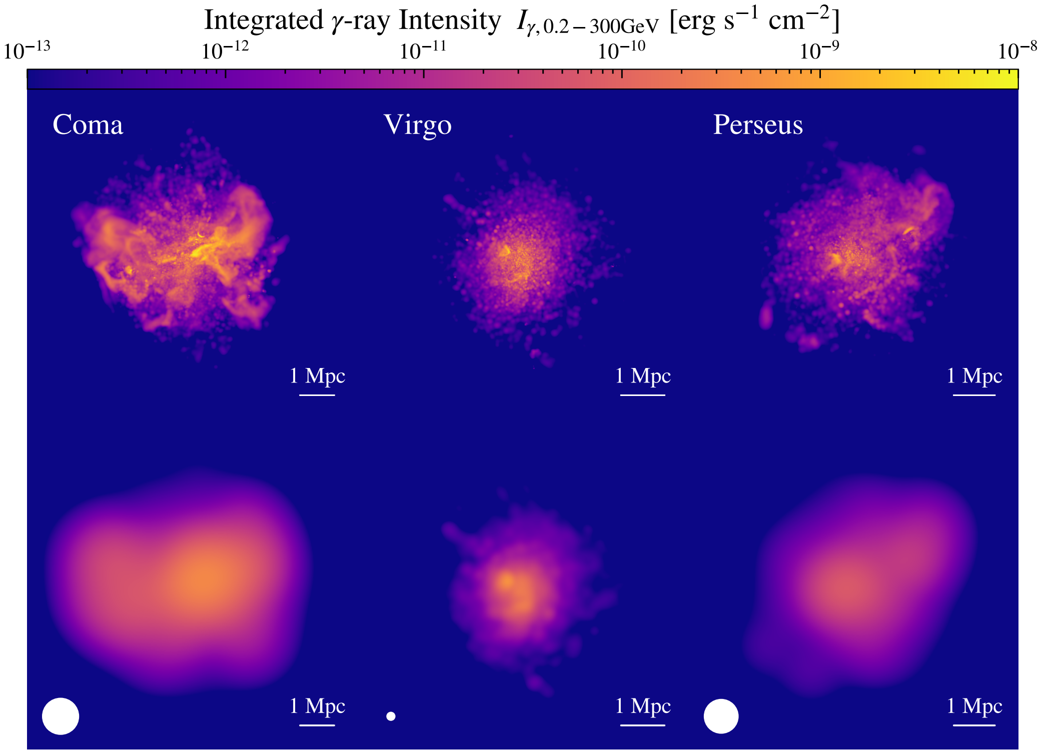

Fig. 4. We show the integrated γ-ray intensity for three prominent clusters. Each image has a width of $3r_{\mathrm{vir}}$ of the respective cluster. The top panels show the simulation output. The bottom panels show the same images as above but smoothed with a Gaussian beam with the single photon angular resolution at 1 GeV of $\theta = 0.6°$ of the Fermi-LAT instrument (Atwood et al. 2009). The white circle in the lower-left corner indicates the size of $\theta = 0.6°$ at the observed redshift of the cluster.

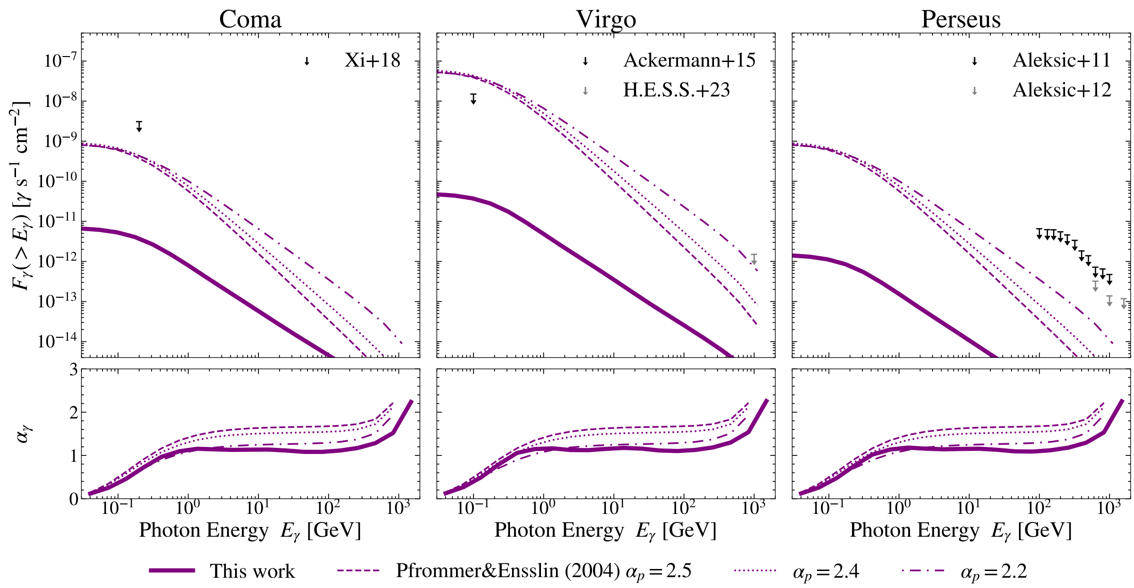

Fig. 5. Integrated γ-ray spectra for our three selected clusters: Coma, Virgo and Perseus. Solid lines show our results, while arrows indicate the upper limits from observations, where available. Different dashed lines show the results from applying the model by Pfrommer & Enßlin (2004) for a fixed $X_{\mathrm{cr}} = 0.01$ under varying proton energy slopes α_p.

lines show the model by Pfrommer & Enßlin (2004) with a fixed $X_{\mathrm{cr}} = 0.01$. Here, dashed lines show the result for a proton energy spectrum with slope $\alpha_p = 2.5$, dotted lines with $\alpha_p = 2.4$, and dashed-dotted lines with $\alpha_p = 2.2$.

In general, we find a consistent picture to Fig. 2. Our spectra show fluxes 2-3 orders of magnitude below the observational limits.

Like Pinzke et al. (2011), we find a universal γ-ray slope for energies above 1 GeV. They find a spectral slope of the γ-ray flux which scales as $\alpha_\gamma \approx -1.2$, corresponding to a mean energy slope of $\alpha_p \approx 2.2$.

In our simulation, however we find a spectral slope of the γ-ray

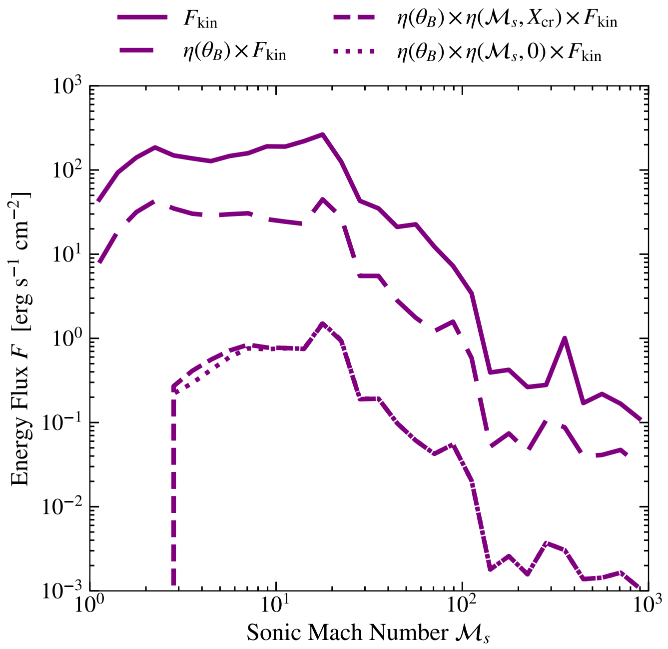

Fig. 6. Histograms of the dissipated energy. The solid line shows the total kinetic energy flux as identified in the shock finder. The long dashed line shows the energy flux available for CR proton acceleration when accounting for the shock obliquity-dependent acceleration model $\eta(\theta_B)$. The short dashed line shows the energy flux available for CR acceleration when accounting for $\eta(\theta_B)$ and re-acceleration of protons as a function of the sonic Mach number. The dotted line shows the same as the dashed line when only accounting for the acceleration of protons from the thermal pool.

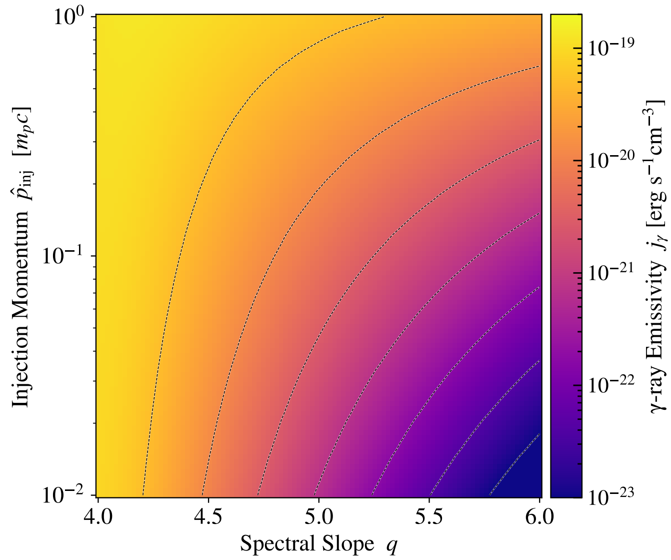

Fig. 7. γ-ray emissivity as a function of spectral slope q and injection momentum $\hat{p}_{\rm inj}$ for a fixed total energy density in CR protons. The dashed lines show contours spaced by half an order of magnitude.

flux of $\alpha_\gamma \approx -1$, which indicates a mean energy slope for the proton population of $\alpha_p \approx 2.0$. This is the limit for spectra accelerated by DSA. We attribute this again to the resolution limitations of our shock finder. As we showed in Paper I and will discuss in Sec. 6.1, the resolution of the cosmological box is not sufficient to capture all low Mach number shocks in the ICM. We are instead biased to stronger shocks, which lead to flatter CR spectra.

6. Discussion

6.1. Impact of Shock Finder Accuracy

Since DSA is the only source of CRs in our simulation the accuracy of the injected CR population depends strongly on the performance of the shock finder. To illustrate the impact of the performance by our shock finder, we compute the dissipated energy available for CR proton acceleration as in Ryu et al. (2003)

$$F_{\rm CR} = \eta(\mathcal{M}_s, X_{\rm cr}, \theta_B) \times F_{\rm kin} = \frac{1}{2}\,\eta(\mathcal{M}_s, X_{\rm cr}, \theta_B)\,\rho_u\,v_s^3\,, \qquad (14)$$

where v_s is the shock velocity, ρ_u the upstream density and $\eta(\mathcal{M}_s, X_{\rm cr}, \theta_B)$ the acceleration efficiency. In Fig. 6 we show the histogram of dissipated energy as a function of sonic Mach number for the whole simulation domain. The solid line shows the total dissipated energy.

We find that due to resolution constraints, the shock finder does not capture all low Mach number shocks in the clusters, as can be seen by the lower end of the histogram. Compared to work by Ryu et al. (2003); Schaal & Springel (2015); Banfi et al. (2020), we find that the dissipated energy decreases below $\mathcal{M}_s \sim 20$, while in the previous works, the majority of the energy dissipated at shock lies in the range $\mathcal{M}_s \leq 5$. From their histograms, we estimate a factor of $\sim 1-2$ orders of magnitude under-prediction of the dissipated energy in this low Mach number range. This energy is dissipated in the code and heats the gas, it is just not necessarily captured by the shock finder, which leads to an under-injection of CR protons.

Another impact of the shock finder on our results is due to our inclusion of a shock obliquity-dependent efficiency model. As already discussed in Paper I, we find shock obliquities that are biased towards high obliquity shocks (see Paper I, Fig. 9). This stems from the shock finder capturing a numerically broadened shock. As the shock propagates through the medium, only the perpendicular component of the magnetic field is compressed, leading to an alignment of the shock surface and magnetic field vector. In our numerically broadened shock, we also capture the decaying flank of the Mach number distribution, in which the magnetic field is already preferentially aligned with the shock surface. This, together with our description for $\eta(\theta_B)$, leads to an artificial suppression of CR proton accelerations. As can be seen in the dashed line of Fig. 6, the mean value of $\eta(\theta_B) \sim 0.1-0.2$ reduces the available energy for CR proton acceleration by a factor 5-10.

We will discuss the remainder of Fig. 6 in the following sections.

6.2. Impact of CR Injection Parameters

As in Paper I we want to briefly discuss the choice of CR injection parameters on our results. For protons the relevant parameters are the injection momentum $p_{\rm inj}$, the injection slope $q_{\rm inj}$ and the overall acceleration efficiency $\eta(\mathcal{M}_s, X_{\rm cr}, \theta_B)$.

6.2.1. Injection Momentum $\hat{p}_{\rm inj}$

For this work, we used a fixed injection momentum of $\hat{p}_{\rm inj} = 0.1$. In other recent work (e.g. Ha et al. 2020) the injection momentum is computed on-the-fly as

$$\hat{p}_{\rm inj,p} = \xi \frac{p_{\rm th,p}}{m_p c} = 3.0 - 3.5 \, \frac{\sqrt{2 k_B m_p T_2}}{m_p c} \tag{15}$$

where T_2 is the temperature downstream of the shock and we used $\xi \approx 3.0 - 3.5$ from Ryu et al. (2019). Compared to the impact of $p_{\rm inj}$ on synchrotron emission, the impact in γ-ray production is quite significant, as can be seen in Fig. 7. Here we show the emissivity of a CR proton population with a fixed total energy in the parameter space of injection momentum and spectral slope. The color code indicates the emissivity per parameter space element and contours indicate changes by half an order of magnitude.

For strong shocks where $q \sim 4$, the difference between $p_{\rm inj} = 0.01$ and $p_{\rm inj} = 1$ only leads to an insignificant change in emissivity. This changes drastically, however, when considering shocks of $\mathcal{M}_s \approx 3$ and with that $q = 4.5$. These weak shocks are expected in the cluster periphery where they are visible as radio relics (see van Weeren et al. 2019, for a recent review). At a slope of $q = 4.5$, we find a reduction of two orders of magnitude in emissivity for an equal reduction in $p_{\rm inj}$. For $\mathcal{M}_s \approx 2$ shocks with $q = 5$ this discrepancy even increases to three orders of magnitude. As these CR protons are accelerated even further in the cluster center and can therefore advect in the cluster volume, this has strong implications for the total γ-ray emission. We note however, that our conservative approach to using a fixed injection momentum of $\hat{p}_{\rm inj} = 0.1$ leads to an increased emission compared to typical values of $\hat{p}_{\rm inj}$ when computed directly from Eq. 15.

We will study the impact of varying $p_{\rm inj}$ in future zoom-in simulations at 8x the current resolution where we can expect our shock finder to be fully converged.

6.2.2. Injection Slope $q_{\rm inj}$

The strong dependence of γ-ray emissivity on q also has implications for the parametrization of $q_{\rm inj}$. As discussed in Paper I, in recent work by Caprioli et al. (2020), the authors find a magnetosonic post-cursor wave that can efficiently scatter particles from the shock acceleration region. The development of this wave depends on the ratio between the downstream Alfvén velocity $v_{A,2}$ and the downstream velocity u_2. This modifies $q_{\rm inj}$ to

$$q_{\rm inj} = \frac{3r}{r - 1 - \alpha}; \;\; \alpha \equiv \frac{v_{A,2}}{u_2} \tag{16}$$

where r is the shock compression ratio.

For the low Mach number shocks in the ICM, even small values for α with $\alpha \leq 0.2$ can have a significant impact on the injection slope. As can be seen in Fig. 7 for our fixed value of $\hat{p}_{\rm inj} = 0.1$, a steepening of the spectrum by 0.5 or 1 leads to a decrease of half an order or one order of magnitude in emissivity, respectively.

However, this parametrization was found for low-β supernova shocks, which expand into a medium that is vastly different than the high-β ICM considered here. There is currently no work in the literature that explores the dependence $q_{\rm inj}(\alpha)$.

6.2.3. Acceleration Efficiency $\eta(\mathcal{M}_s, X_{\rm cr}, \theta_B)$

For this work, we employ the DSA parametrization of Ryu et al. (2019), which shows a weak dependence on sonic Mach number $\mathcal{M}_s$ for CR proton acceleration from the thermal pool. The re-acceleration efficiency is slightly larger, as can be seen, e.g. in Fig. 6, however, our injection model interpolates between acceleration and re-acceleration based on the value of $X_{\rm cr}$ currently in present in the SPH particle and the reference value for $X_{\rm cr}$ in the model, which in the case of Ryu et al. (2019) is $X_{\rm cr} = 0.05$. Since the initial acceleration from the thermal pool is so inefficient for low Mach number shocks, we rarely reach these values, as can be seen in the top panel of Fig. 2. This leads to our model being driven by initial acceleration, rather than re-acceleration.

However, the Ryu et al. (2019) model only allows for acceleration of particles beyond $\mathcal{M}_s = 2.25$, narrowing the range of available shocks to accelerate CRs significantly.

Previous work by Aleksić et al. (2010); Pinzke & Pfrommer (2010) use efficiency models that reach 50% at strong shocks and decreases to 4% at $\mathcal{M}_s \approx 1.7$ (Enßlin et al. 2007). Compared to our parametrization of the Ryu et al. (2019) model, this is a factor of 20 higher for strong shocks and almost one order of magnitude higher for weak shocks. Together with the shock obliquity-dependent acceleration model, which is absent in these works, this can account for a discrepancy of two orders of magnitude in γ-ray emission from CR protons accelerated at weak shocks in galaxy clusters.

Recent simulations by Orusa et al. (2025) indicate, that in 3D also quasi-perpendicular shocks can accelerate CR protons, unlike in our modelling of shock obliquity dependent acceleration based on Caprioli & Spitkovsky (2014); Pais et al. (2018). This could increase the γ-ray emission in our simulation by another factor of 5-10.

6.3. Impact of Cosmic Ray Transport

The nature and propagation velocity of CR transport in the ICM are still strongly under debate. The two most common flavors of CR transport are CR diffusion, where CRs propagate along magnetic field lines with a constant, or energy-dependent diffusion coefficient, or CR streaming where CRs stream down a CR pressure gradient with a streaming velocity $v_{\rm st}$ which generally depends on the magnetic field strength and density in the medium and is of the order of the Alfvén, or sound speed (see e.g. Enßlin et al. 2011, for a detailed discussion). With the long cooling times of CR protons, it can be expected that, independent of the exact nature of these transport processes, CR protons will fill the entire cluster volume over the Hubble time.

Including CR transport in simulations adds a significant numerical challenge and cost (see Hanasz et al. 2021, for a recent review), which made it unfeasible for this large cosmological simulation. Due to the Lagrangian nature of our simulation code, however, we automatically account for the advection of CRs, which is expected to be the dominant transport process for low-energy CR protons (Enßlin et al. 2011; Wiener et al. 2013, 2018; Reichherzer et al. 2025).

We expect the potential inclusion of streaming to reduce the γ-ray flux from the center of the cluster, as CR protons would stream down the CR pressure gradient towards the cluster periphery.

The inclusion of diffusion could potentially impact the expected γ-ray emission, given that the diffusion coefficient is energy-dependent. Assuming that higher energy protons diffuse faster/easier would lead to a flattening of the CR proton spectrum away from acceleration zones (see e.g. Girichidis et al. 2020, for a study of the evolution of CR proton spectra under anisotropic, energy-dependent diffusion). This would naturally flatten the γ-ray spectrum as well.

However, full cosmological simulations of galaxy clusters, including anisotropic and energy-dependent diffusion, are not computationally feasible as of yet. It could nonetheless hold interesting prospects for future work.

7. Conclusions

In this work, we showed results from the first constrained cosmological simulation with an on-the-fly spectral cosmic ray model to study the time evolution of CR protons in the local Cosmic Web. Our results can be summarized as follows:

– We find CR proton acceleration at structure formation and accretion shocks in and around galaxy clusters and cosmic web filaments.
– The CR protons advect through the cluster and filament volume and settle into halos extending to the virial radius of clusters.
– These protons produce volume-filling, diffuse γ-ray emission on cluster scales through hadronic interactions.
– Strong shocks produce γ-ray emission with surface brightnesses roughly one order of magnitude below the central surface brightness.
– In general, we find values for the CR to thermal pressure ratio ($X_{\rm cr}$) three orders of magnitude below current estimates when averaging over the full cluster volume. This is however partly driven by a lack of resolution for the on-the-fly shock finder, which can account for a missing two orders of magnitude in detected dissipated energy at low Mach number shocks.
– This discrepancy in $X_{\rm cr}$ translates to our predictions for diffuse γ-ray flux and luminosity lying three to five orders of magnitude below the current Fermi-LAT limits.

Future work will have to address the resolution limitation of our shock finder by performing higher-resolution zoom-in simulations of individual clusters. This will also allow us to vary CR acceleration parameters to provide a more conclusive prediction for diffuse γ-ray emission from galaxy clusters.

Acknowledgements. LMB would like to thank Maria Werhahn, Damiano Caprioli, Sruthiranjani Ravikularaman and Jonathan Biteau for helpful discussions. LMB, IK, DK, KD and EH acknowledge support by the Excellence Cluster ORIGINS which is funded by the Deutsche Forschungsgemeinschaft (DFG, German Research Foundation) under Germany's Excellence Strategy - EXC-2094-390783311 and the COMPLEX project from the European Research Council (ERC) under the European Union's Horizon 2020 research and innovation program grant agreement ERC-2019-AdG 882679. LMB is supported by NASA through grant 80NSSC24K0173. The simulations used in this work were carried out at the Leibniz Supercomputer Center (LRZ) under the project *pn68na*. The analysis has been carried out on the computing facilities of the Computational Center for Particle and Astrophysics (C2PAP) and of the Leibniz Supercomputer Center (LRZ).

References

Abe, K., Abe, S., Acero, F., et al. 2024, J. Cosmology Astropart. Phys., 2024, 004
Acciari, V. A., Agudo, I., Aniello, T., et al. 2023, A&A, 670, A145
Ackermann, M., Ajello, M., Albert, A., et al. 2014, ApJ, 787, 18
Ackermann, M., Ajello, M., Albert, A., et al. 2016, ApJ, 819, 149
Ackermann, M., Ajello, M., Albert, A., et al. 2015, ApJ, 812, 159
Adam, R., Goksu, H., Brown, S., Rudnick, L., & Ferrari, C. 2021, A&A, 648, A60
Adam, R., Goksu, H., Leingärtner-Goth, A., et al. 2020, A&A, 644, A70
Aleksić, J., Alvarez, E. A., Antonelli, L. A., et al. 2012, A&A, 541, A99
Aleksić, J., Antonelli, L. A., Antoranz, P., et al. 2010, ApJ, 710, 634
Alves Batista, R. & Saveliev, A. 2020, ApJ, 902, L11
Alves Batista, R. & Saveliev, A. 2021, Universe, 7, 223
Alves Batista, R., Saveliev, A., Sigl, G., & Vachaspati, T. 2016, Phys. Rev. D, 94, 083005
Arth, A., Dolag, K., Beck, A. M., Petkova, M., & Lesch, H. 2014, arXiv e-prints, arXiv:1412.6533
Atwood, W. B., Abdo, A. A., Ackermann, M., et al. 2009, ApJ, 697, 1071
Baghmanyan, V., Zargaryan, D., Aharonian, F., et al. 2022, MNRAS, 516, 562
Banfi, S., Vazza, F., & Wittor, D. 2020, MNRAS, 496, 3648
Beck, A. M., Murante, G., Arth, A., et al. 2016, MNRAS, 455, 2110
Blasi, P., Gabici, S., & Brunetti, G. 2007, International Journal of Modern Physics A, 22, 681
Böhringer, H. & Werner, N. 2010, A&A Rev., 18, 127
Bonafede, A., Dolag, K., Stasyszyn, F., Murante, G., & Borgani, S. 2011, MNRAS, 418, 2234
Böss, L. M., Dolag, K., Steinwandel, U. P., et al. 2024, A&A, 692, A232
Böss, L. M., Steinwandel, U. P., & Dolag, K. 2023a, ApJ, 957, L16
Böss, L. M., Steinwandel, U. P., Dolag, K., & Lesch, H. 2023b, MNRAS, 519, 548
Brüggen, M., Bykov, A., Ryu, D., & Röttgering, H. 2012, Space Sci. Rev., 166, 187
Brunetti, G. & Jones, T. W. 2014, International Journal of Modern Physics D, 23, 1430007
Brunetti, G. & Lazarian, A. 2007, MNRAS, 378, 245
Bykov, A. M., Vazza, F., Kropotina, J. A., Levenfish, K. P., & Paerels, F. B. S. 2019, Space Sci. Rev., 215, 14
Caprioli, D., Haggerty, C. C., & Blasi, P. 2020, ApJ, 905, 2
Caprioli, D. & Spitkovsky, A. 2014, ApJ, 783, 91
Chen, W., Chowdhury, B. D., Ferrer, F., Tashiro, H., & Vachaspati, T. 2015, MNRAS, 450, 3371
Cullen, L. & Dehnen, W. 2010, MNRAS, 408, 669
Dehnen, W. & Aly, H. 2012, MNRAS, 425, 1068
Di Gennaro, G., van Weeren, R. J., Hoeft, M., et al. 2018, ApJ, 865, 24
Dolag, K., Grasso, D., Springel, V., & Tkachev, I. 2005a, J. Cosmology Astropart. Phys., 2005, 009
Dolag, K., Kachelrieß, M., Ostapchenko, S., & Tomàs, R. 2009, The Astrophysical Journal, 703, 1078
Dolag, K., Sorce, J. G., Pilipenko, S., et al. 2023, A&A, 677, A169
Dolag, K., Vazza, F., Brunetti, G., & Tormen, G. 2005b, MNRAS, 364, 753
Doumler, T., Courtois, H., Gottlöber, S., & Hoffman, Y. 2013a, MNRAS, 430, 902
Doumler, T., Gottlöber, S., Hoffman, Y., & Courtois, H. 2013b, MNRAS, 430, 912
Doumler, T., Hoffman, Y., Courtois, H., & Gottlöber, S. 2013c, MNRAS, 430, 888
Enßlin, T., Pfrommer, C., Miniati, F., & Subramanian, K. 2011, A&A, 527, A99
Enßlin, T. A., Pfrommer, C., Springel, V., & Jubelgas, M. 2007, A&A, 473, 41
Girichidis, P., Pfrommer, C., Hanasz, M., & Naab, T. 2020, MNRAS, 491, 993
Górski, K. M., Hivon, E., Banday, A. J., et al. 2005, ApJ, 622, 759
Groth, F., Steinwandel, U. P., Valentini, M., & Dolag, K. 2023, MNRAS, 526, 616
H. E. S. S. Collaboration, Aharonian, F., Ait Benkhali, F., et al. 2023, A&A, 675, A138
Ha, J.-H., Ryu, D., & Kang, H. 2020, ApJ, 892, 86
Ha, J.-H., Ryu, D., & Kang, H. 2023, ApJ, 943, 119
Ha, J.-H., Ryu, D., Kang, H., & van Marle, A. J. 2018, ApJ, 864, 105
Hanasz, M., Strong, A. W., & Girichidis, P. 2021, Living Reviews in Computational Astrophysics, 7, 2
Hernández-Martínez, E., Dolag, K., Seidel, B., et al. 2024, A&A, 687, A253
Hoffman, Y. & Ribak, E. 1991, ApJ, 380, L5
Hopkins, P. F., Butsky, I. S., Panopoulou, G. V., et al. 2022, MNRAS, 516, 3470
Jubelgas, M., Springel, V., & Dolag, K. 2004, MNRAS, 351, 423
Kafexhiu, E., Aharonian, F., Taylor, A. M., & Vila, G. S. 2014, Phys. Rev. D, 90, 123014
Kang, H. & Jones, T. W. 2007, Astroparticle Physics, 28, 232
Kang, H. & Ryu, D. 2013, ApJ, 764, 95
Lebeau, T., Sorce, J. G., Aghanim, N., Hernández-Martínez, E., & Dolag, K. 2024, A&A, 682, A157
Miniati, F. 2001, Computer Physics Communications, 141, 17
Neronov, A. & Semikoz, D. V. 2007, Soviet Journal of Experimental and Theoretical Physics Letters, 85, 473
Neronov, A. & Semikoz, D. V. 2009, Phys. Rev. D, 80, 123012
Orusa, L., Caprioli, D., Sironi, L., & Spitkovsky, A. 2025, arXiv e-prints, arXiv:2507.13436
Pais, M., Pfrommer, C., Ehlert, K., & Pakmor, R. 2018, MNRAS, 478, 5278
Pfrommer, C. & Enßlin, T. A. 2004, A&A, 413, 17
Pinzke, A. & Pfrommer, C. 2010, MNRAS, 409, 449
Pinzke, A., Pfrommer, C., & Bergström, L. 2011, Phys. Rev. D, 84, 123509
Plaga, R. 1995, Nature, 374, 430
Planck Collaboration, Ade, P. A. R., Aghanim, N., et al. 2014, A&A, 571, A16
Prokhorov, D. A. & Churazov, E. M. 2014, A&A, 567, A93
Reichherzer, P., Bott, A. F. A., Ewart, R. J., et al. 2025, Nature Astronomy, 9, 438
Ryu, D., Kang, H., & Ha, J.-H. 2019, ApJ, 883, 60

Ryu, D., Kang, H., Hallman, E., & Jones, T. W. 2003, ApJ, 593, 599
Schaal, K. & Springel, V. 2015, MNRAS, 446, 3992
Skillman, S. W., Xu, H., Hallman, E. J., et al. 2013, ApJ, 765, 21
Sorce, J. G. 2015, MNRAS, 450, 2644
Sorce, J. G. 2018, MNRAS, 478, 5199
Sorce, J. G., Courtois, H. M., Gottlöber, S., Hoffman, Y., & Tully, R. B. 2014, MNRAS, 437, 3586
Sorce, J. G., Hoffman, Y., & Gottlöber, S. 2017, MNRAS, 468, 1812
Sorce, J. G. & Tempel, E. 2017, MNRAS, 469, 2859
Sorce, J. G. & Tempel, E. 2018, MNRAS, 476, 4362
Springel, V. 2005, MNRAS, 364, 1105
Stecker, F. W. 1971, 1, Vol. 249, Cosmic gamma rays
Stroe, A., Shimwell, T., Rumsey, C., et al. 2016, MNRAS, 455, 2402
Stroe, A., van Weeren, R. J., Intema, H. T., et al. 2013, A&A, 555, A110
Tricco, T. S., Price, D. J., & Bate, M. R. 2016, Journal of Computational Physics, 322, 326
Tully, R. B., Courtois, H. M., Dolphin, A. E., et al. 2013, AJ, 146, 86
van Weeren, R. J., de Gasperin, F., Akamatsu, H., et al. 2019, Space Science Reviews, 215
Vazza, F., Brüggen, M., Wittor, D., et al. 2016, MNRAS, 459, 70
Vazza, F., Dolag, K., Ryu, D., et al. 2011, MNRAS, 418, 960
Werhahn, M., Girichidis, P., Pfrommer, C., & Whittingham, J. 2023, MNRAS, 525, 4437
Werhahn, M., Pfrommer, C., Girichidis, P., & Winner, G. 2021, MNRAS, 505, 3295
Wiener, J., Oh, S. P., & Guo, F. 2013, MNRAS, 434, 2209
Wiener, J., Zweibel, E. G., & Oh, S. P. 2018, MNRAS, 473, 3095
Wittor, D. 2021, New Astronomy, 85, 101550
Wittor, D., Vazza, F., & Brüggen, M. 2017, MNRAS, 464, 4448
Xi, S.-Q., Wang, X.-Y., Liang, Y.-F., et al. 2018, Phys. Rev. D, 98, 063006
Yang, R.-z., Kafexhiu, E., & Aharonian, F. 2018, A&A, 615, A108
Zaroubi, S., Hoffman, Y., Fisher, K. B., & Lahav, O. 1995, ApJ, 449, 446
Zaroubi, S., Squires, G., Hoffman, Y., & Silk, J. 1998, ApJ, 500, L87
Zhang, C., Churazov, E., Dolag, K., Forman, W. R., & Zhuravleva, I. 2020a, MNRAS, 498, L130
Zhang, C., Churazov, E., Dolag, K., Forman, W. R., & Zhuravleva, I. 2020b, MNRAS, 494, 4539

Appendix A: Gamma-Ray Emission from CR momentum spectra

As mentioned in Sec. 2.4 our computation of the γ-ray emissivity closely follows the method described in Werhahn et al. (2021), see their Appendix 1. With the difference that we only use the parametrization by Kafexhiu et al. (2014), and omit the inclusion of Yang et al. (2018) for low CR energies. We will summarize the core concepts here, for completeness.
The emissivity of a momentum distribution of a CR proton spectrum $f(\hat{p})$ is given in Eq. 4 and repeated here:

$$q_\gamma(E_\gamma) = 4\pi c\, n_H \int_{\hat{p}_{\rm thr}}^{\hat{p}_{\rm max}} {\rm d}\hat{p}\;\; \hat{p}^2\; f(\hat{p})\; \frac{{\rm d}\sigma_\gamma(E_\gamma,\hat{p})}{{\rm d}E_\gamma} \tag{A.1}$$

The central task of this computation is the differential cross-section of π-on production, which takes the general form

$$\frac{{\rm d}\sigma_\gamma(E_\gamma, E_p)}{{\rm d}E_\gamma} = 2\int_{E_{\pi,{\rm min}}}^{E_{\pi,{\rm max}}} {\rm d}E_\pi \frac{{\rm d}\sigma_\pi(E_p, E_\pi)}{{\rm d}E_\pi} f_{\gamma,\pi}(E_\gamma, E_\pi) \tag{A.2}$$

where the normalized energy distribution $f_{\gamma,\pi}(E_\gamma, E_\pi)$ is a Green's function which describes the probability for a pion at energy E_π to produce a γ photon at energy E_γ, where

$$f_{\gamma,\pi}(E_\gamma, E_\pi) = \frac{1}{\sqrt{E_\pi^2 - E_{\pi,0}^2}} \tag{A.3}$$

following Stecker (1971). In the absence of an analytic solution for Eq. A.3, Kafexhiu et al. (2014) introduce the parametrisation

$$\frac{{\rm d}\sigma_\gamma(E_\gamma,\hat{p})}{{\rm d}E} = A_{\rm max}(T_p(\hat{p}))\; F(T_p(\hat{p}), E_\gamma) \tag{A.4}$$

The peak of the differential cross-section $A_{\rm max}(E_p)$ can be expressed as

$$A_{\rm max}(E_p) = \begin{cases} b_0 \times \frac{\sigma_{\rm pp,inel}(E_p)}{E_\pi^{\rm max}}, & \text{for } E_p^{\rm th} \leq E_p \leq 1\ \text{GeV} \\ b_1\, \theta_p^{-b_2}\; e^{(b_3 \log^2(\theta_p))} & \\ \times \frac{\sigma_{\rm pp,inel}(E_p)}{E_{p,0}}, & \text{for } E_p \geq 1\ \text{GeV} \end{cases} \tag{A.5}$$

where b_i are fit parameters to Geant4 data, $E_\pi^{\rm max}$ is the maximum π-on energy in the lab frame allowed by the participating particle's kinematics, and $E_{p,0}$ is the proton rest mass. $\sigma_{\rm pp,inel}(E_p)$ is the inclusive π^0 production cross section given as

$$\sigma_{\rm pp,inel}(T_p) = \left[30.7 - 0.96\log\left(\frac{T_p}{T_{p,{\rm th}}}\right) + 0.18\log^2\left(\frac{T_p}{T_{p,{\rm th}}}\right)\right] \tag{A.6}$$

$$\times\left[1 - \left(\frac{T_p}{T_{p,{\rm th}}}\right)^{1.9}\right]^3\ {\rm mb} \tag{A.7}$$

where T_p is the kinetic energy of the proton in the lab frame and $T_{p,{\rm th}} = 2m_\pi c^2 + m_\pi^2 c^4/(2m_p c^2) \approx 0.2797$ GeV is the threshold proton kinetic energy in the particle lab frame.
The fit formula $F(E_p, E)$ in Eq. A.4 can be written as

$$F(E_p, E_\gamma) = \frac{\left(1 - X_\gamma^{\alpha(E_p)}\right)^{\beta(E_p)}}{\left(1 + \frac{X_\gamma}{C}\right)^{\gamma(E_p)}} \tag{A.8}$$

where $\alpha(E_p)$, $\beta(E_p)$, and $\gamma(E_p)$ are fit functions, which we will omit in the interest of brevity, that depend on the proton energy in the lab frame E_p. X_γ is a ratio between the energy of the emitted γ-photon, the maximum allowed γ-photon energy and the rest-mass of a π-on.

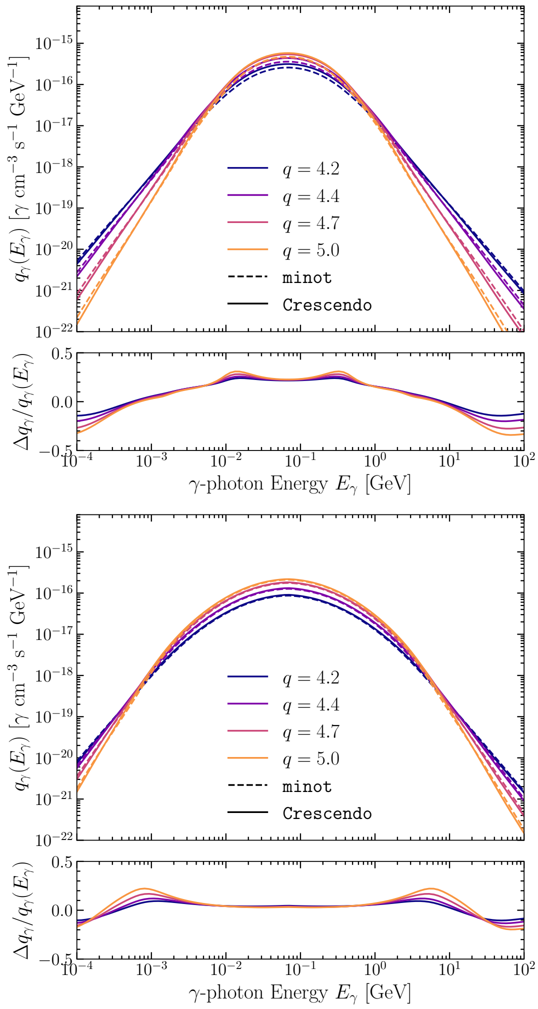

Fig. B.1. We compare our calculations of the γ-ray source function to the one by the minot package. For both plots we set up a powerlaw in momentum space with an energy density of $\epsilon_{{\rm CR},p} = 1$ erg cm^{-3} and vary the minimum momentum of the powerlaw $p_{\rm min}$. *Top panels:* $p_{\rm min} = 1\ \frac{\rm GeV}{c}$. *Bottom panels:* $p_{\rm min} = 10\ \frac{\rm GeV}{c}$.

Appendix B: Tests for γ-emission

In Fig. B.1 we show the results of our calculation of the γ-ray source function as a function of photon energy E_γ. To calculate the source function we set up powerlaws in momentum space with varying slope q. Between the panels we vary the minimum momentum $p_{\rm min}$ at which the powerlaw starts. For the top panel this is $p_{\rm min} = 1$ GeV c^{-1} and for the bottom panel $p_{\rm min} = 10$ GeV c^{-1}. The maximum momentum is fixed at $p_{\rm max} = 10^5$ GeV c^{-1}. Each powerlaw is normalized to contain a CR proton energy density of $\epsilon_{{\rm CR},p} = 1$ erg cm^{-3}. As in the simulation we discretize the spectrum with a total of 12 bins in either case. To improve convergence we sub-sample the spectrum by a factor of 10 in momentum space. We only consider proton-proton collisions for the pion production, thus neglecting the impact of heavier nuclei on the resulting γ-ray spectrum, and compare our results to the minot package (Adam et al. 2020). In general, we find reasonable agreement between the two implementations with the slight discrepancy originating from a difference in the low-momentum treatment between Crescendo and minot caused by solving the emission from a power-law in momentum- and energy space, respectively.